Journal of Materials Chemistry A

ROYAL SOCIETY OF CHEMISTRY

REVIEW

View Article Online
View Journal

Cite this: DOI: 10.1039/d5ta03551a

Surface modification strategies for direct methane and direct ammonia solid oxide fuel cell anodes: current approaches and future directions

Hao-Yang Li,[ab] Hyunseung Kim,[ab] Jeong Woo Shin,[a] Jiyoon Shin[a] and Pei-Chen Su *[ab]

Solid oxide fuel cells (SOFCs) offer high efficiency and fuel flexibility for next-generation energy conversion, yet direct utilization of methane and ammonia remains hindered by anode degradation from carbon coking, nitridation, and sluggish reaction kinetics in conventional Ni-based cermets. This review systematically examines surface modification strategies, specifically infiltration, exsolution, and atomic layer deposition (ALD), to enhance anode stability and performance. Emphasis is placed on ALD as an emerging, transformative technique, prized for its atomic-level precision, superior conformality over complex porous architectures, and ability to achieve low catalyst loading with controllable uniformity—challenges that conventional methods often struggle to address. Comparative literature analysis confirms that ALD surface modifications enhance anode performance and stability more effectively than infiltration (nonuniform) or exsolution (limited tunability) by enabling precise engineering of triple-phase boundaries and protective interfaces. Looking forward, scalable ALD processes, multifunctional multilayers, and hybrid integrations are identified as key avenues for enabling the commercialization of durable, direct-fueled SOFCs.

Received 5th May 2025
Accepted 21st January 2026

DOI: 10.1039/d5ta03551a

rsc.li/materials-a

1. Introduction

Solid oxide fuel cells (SOFCs) are promising next-generation energy conversion devices offering high efficiency (~60%) and fuel flexibility, as well as ease of coupling with electrical loads.[1–7] SOFCs can be generally categorized according to the nature of their ion-conducting electrolyte. Oxide-ion conducting SOFCs (O-SOFCs) typically employ materials such as yttria-stabilized zirconia (YSZ) or gadolinium-doped ceria (GDC), and proton-conducting SOFCs (H-SOFCs or PCFCs) utilize materials such as $Ba(Zr,Ce,Y,Yb)O_{3-\delta}$ (BZCYYb) for their electrolytes.

While hydrogen is considered the ideal fuel for both types of SOFCs, its widespread adoption is limited by storage, compression, and transportation challenges.[8,9] The relatively

[a]School of Mechanical and Aerospace Engineering, Nanyang Technological University, 50 Nanyang Avenue, Singapore 639798, Singapore

[b]Energy Research Institute @ NTU (ERI@N), Interdisciplinary Graduate School, Nanyang Technological University, 50 Nanyang Avenue, Singapore 637553, Singapore

Hao-Yang Li

Hao-Yang Li received his doctoral degree from the School of Mechanical and Aerospace Engineering at Nanyang Technological University (NTU) and is currently conducting his research as a postdoctoral research fellow at Energy Research Institute @ NTU (ERI@N), Nanyang Technological University, Singapore. His research interests focus on functional ceramic materials and energy conversion devices, specifically solid oxide cells.

Hyunseung Kim

Hyunseung Kim received his doctoral degree from the Department of Materials Science and Engineering, Korea Advanced Institute of Science and Technology (KAIST), and is currently pursuing his research as a postdoctoral research fellow at Energy Research Institute @ NTU (ERI@N), Nanyang Technological University, Singapore. His research interests primarily focus on gas/solid interfaces, solid oxide fuel cells, and surface Sr segregation.

high operating temperature of SOFCs (>650 °C for O-SOFCs and >450 °C for H-SOFCs) allows the use of hydrogen carrier fuels such as methane and ammonia, which benefit from well-established production and distribution infrastructure with high energy density.[10–12]

SOFCs employ two primary strategies for utilizing these fuels: indirect and direct fueling. In the indirect approach, methane or ammonia is externally reformed to hydrogen, simplifying anodic reactions but increasing system cost and complexity.[13,14] Conversely, direct-fueled SOFCs introduce raw methane or ammonia directly into the anode, leveraging the high operating temperature for *in situ* reforming. This eliminates the need for external reformers, reduces system footprint, and enhances overall efficiency; however, it also imposes significant challenges on conversion efficiency and stability.[10–12,15–17]

Current efforts to advance anodes for direct methane (DM-) and direct ammonia (DA-) SOFCs have primarily focused on material optimization to address the severe challenges posed by methane and ammonia as direct fuels.[14,18–23] Conventional Ni-based cermets such as Ni–(Y,Zr)$O_{2-\delta}$ (Ni–YSZ), Ni–(Sm,Ce)$O_{2-\delta}$ (Ni–SDC), and Ni–(Gd,Ce)$O_{2-\delta}$ (Ni–GDC) remain widely employed for their high conductivity and catalytic activity in both hydrogen oxidation reactions and fuel decomposition reactions; however, they still suffer from severe carbon coking in methane and nitridation in ammonia, leading to rapid degradation.[24–34] Alternative strategies, including use of perovskite-based oxides such as $Sr_2Fe_{1.5}Mo_{0.5}O_{6-\delta}$ (SFMO) and $La_{0.75}Sr_{0.25}Cr_{0.5}Mn_{0.5}O_{3-\delta}$ (LSCM),[35–38] metal-alloyed Ni systems (Ni–Fe, Ni–Cu, and Ni–Co),[39–45] and gradient-structured cermets,[46,47] have improved stability but often compromise catalytic activity or scalability. These trade-offs highlight the need for approaches that enhance surface reactivity without altering bulk properties.

For direct-fueled SOFCs, which require anodes that are both electrochemically active and highly reactive/stable toward the decomposition of hydrogen carriers, surface modification has emerged as a particularly promising approach. While preserving the intrinsic electronic conductivity, gas permeability, and hydrogen oxidation activity of conventional electrodes, techniques such as infiltration and exsolution enable precise tuning of catalytic interfaces, which provide a targeted means to mitigate degradation while maintaining structural integrity. Unlike bulk redesign strategies, surface engineering introduces active or protective layers that suppress carbon deposition in DMSOFCs and prevent nickel nitridation in DASOFCs. Moreover, these modifications facilitate incorporation of highly active catalytic species, accelerating fuel oxidation, reducing polarization losses, and extending anode lifetime. Despite extensive application in hydrogen-fueled SOFCs, especially for cathode enhancement, surface modification remains underexplored for directly fueled systems, where its impact could be significant. By tailoring interfacial chemistry, surface engineering provides a scalable, high precision strategy to overcome the fundamental limitations of direct methane and ammonia utilization.

Further promising strategies that exceed conventional surface modification approaches can be realized through the adoption of advanced thin-film deposition techniques, notably atomic layer deposition (ALD). ALD offers a unique capability for atomic-scale regulation of surface composition,

Jeong Woo Shin

Jeong Woo Shin received his doctoral degree from the Department of Energy and Chemical Engineering, Seoul National University of Science and Technology (SeoulTech), and worked as a postdoctoral research fellow at the School of Mechanical and Aerospace Engineering at Nanyang Technological University (NTU). His research interests primarily focus on nanoscale surface engineering by atomic layer deposition for thin film energy devices.

Jiyoon Shin

Jiyoon Shin is currently pursuing her doctoral degree from the School of Mechanical and Aerospace Engineering at Nanyang Technological University (NTU), Singapore. Her research interests focus on surface nanocoating and modification of energy conversion devices, specifically solid oxide cells.

Pei-Chen Su

Professor Pei-Chen Su is an associate professor at the School of Mechanical and Aerospace Engineering and Cluster Director of the Energy Research Institute (ERI@N) at Nanyang Technological University (NTU), Singapore. She is also the vice president of the Thin Films Society. Her research interests primarily focus on surface coating and interfacial modification of energy conversion devices, high-temperature nanoionics, semiconductor processes, and 4D printing.

morphology, and chemical stability, surpassing the limitations of infiltration and exsolution. Owing to its self-limiting gas–solid reaction sequence, ALD delivers exceptional precision and conformality, ensuring uniform coating even on complex and irregular electrode architectures. Moreover, its capacity to form coating layers on Ni particles effectively mitigates carbon coking, while the presence of active and well-dispersed precious metal sites enables rapid ammonia decomposition, and its tunable surface chemistry can further suppress nitridation and other parasitic reactions under fuel-rich conditions.

This review examines the critical challenges of direct methane- and ammonia-fueled SOFC anodes and assesses the potential of thin-film surface modification in addressing these limitations. By highlighting recent advances in these techniques, this work proposes their promise for optimizing anode performance and accelerating the commercialization of direct-fueled SOFCs.

2. Direct-fueled solid oxide fuel cell anodes: challenges & metrics

2.1. Anode requirements and performance targets

For commercial viability, direct-fueled SOFC anodes must meet stringent performance targets, including catalytic activity with polarization resistance <0.2 Ω cm^2, stability *via* degradation rates <0.2% per 1000 hours, fuel utilization >70% to maximize system efficiency, and durability against carbon deposition, sulfur poisoning, and microstructural coarsening. To meet these requirements, the anode must exhibit strong electrochemical activity toward hydrogen oxidation and high thermochemical activity for the decomposition of hydrogen carrier gases. Current Ni-based anodes in direct ammonia and methane SOFCs often exceed these thresholds, exhibiting 1–6% initial losses from nitridation or coking, necessitating the need for advanced surface modifications like ALD to achieve DOE benchmarks of 40 000 h lifetime at ≤$ 225 per kW stack cost.[48]

2.2. Fuel reaction mechanisms: O-SOFCs *vs.* H-SOFCs

Fig. 1 depicts the principal reaction steps occurring within the reformer and anodes of SOFCs directly fueled by methane or ammonia. Under direct fueling conditions, a complex interplay of diverse reactions takes place within the anode. In direct methane-SOFCs (DM-SOFCs), methane undergoes a complex network of reactions that depend on the available oxidizing agents, such as H_2O, O_2, CO_2, or their mixtures (Fig. 1a).[49,50] These include direct electrochemical oxidation of methane, steam reforming, dry reforming, and methane decomposition.[19] The initial C–H bond cleavage represents the rate-limiting step, necessitating highly active catalysts to reduce the activation barrier and enable efficient methane conversion.[18] Subsequent reforming reactions generate H_2 and CO, which are electrochemically oxidized to produce electrons for power generation. However, secondary reactions such as the Boudouard reaction (eqn (1)) promote carbon deposition, compromising anode performance and long-term stability.[51,52]

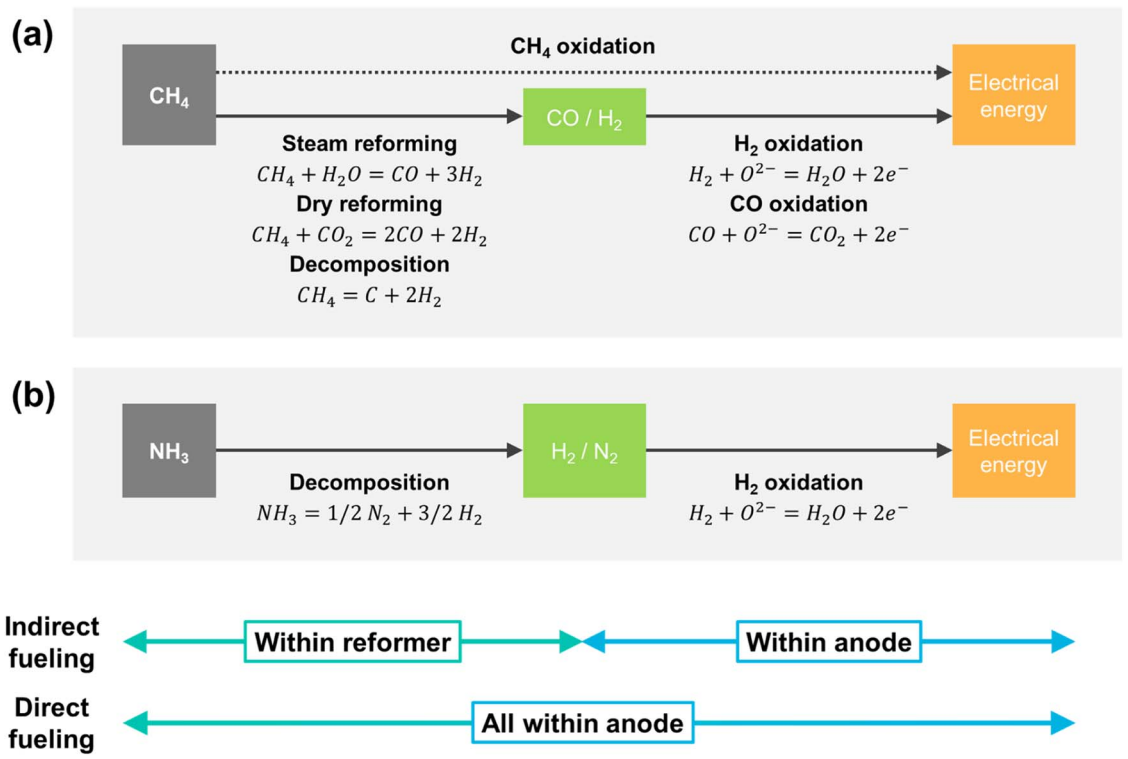

Fig. 1 Schematic representation of the conversion pathways for (a) methane and (b) ammonia in fueling solid oxide fuel cells. For indirect fueling, fuels are reformed or decomposed into hydrogen before entering the anode for hydrogen fuel oxidation, while for direct fueling, both the decomposition and oxidation take place within the anode.

$$2CO{=}C + CO_2 \text{ (Boudouard reaction)} \quad (1)$$

In direct ammonia-SOFCs (DA-SOFCs), ammonia decomposition produces hydrogen and nitrogen, with the hydrogen subsequently undergoing electrochemical oxidation (Fig. 1b).[53–56] The rate-determining step depends on the catalyst's ability to efficiently adsorb and dissociate ammonia while minimizing nitrogen poisoning.[22,23,57] The resulting hydrogen is electrochemically oxidized at the anode, producing water and releasing electrons to sustain the cell reaction. Yet, slow decomposition kinetics and nitrogen-induced nitridation limit reaction rates and durability, while high cracking temperatures and dilution effects increase concentration overpotentials.[14,21–23,35,58–61] Both fuels therefore demand robust anodes capable of catalyzing complex reactions while mitigating degradation pathways.

2.3. Quantitative degradation challenges

In DM-SOFCs, conventional Ni–YSZ anodes suffer severe carbon coking from methane cracking, resulting in rapid performance degradation. Under pure methane at 700 °C, peak power density declined from 0.24 to 0.16 W cm^{-2} within 26 h.[52] Ni–GDC anodes, commonly employed in DM-SOFCs, exhibited voltage decay from 0.7 to 0.55 V over 60 h at constant current.[62] Severe carbon deposition frequently causes cell failure within 30 h (ref. 62) or as little as 8 h.[63] Even highly active Ru–SDC anodes at 450 °C displayed a 3.7%/h degradation rate.[47]

Degradation in DA-SOFCs arises primarily from nickel nitridation in the anode, where nitrogen adsorbed from

Table 1 Comparison of surface modification techniques for SOFC anodes

Technique	Working principle	Advantages	Disadvantages	Features in SOFC application	Improvement
Infiltration	Solution-based precursors impregnate porous scaffolds, followed by calcination to yield nanoparticles	Simple, low-cost, broad material selection	Poor uniformity, nanoparticle agglomeration, weak adhesion, limited reproducibility	Effective for lab-scale activity enhancement, constrained by long-term stability	Power density: 1.1× increase in NH_3 (1.86 W cm^{-2} to 2.062 W cm^{-2} at 700 °C); degradation rate: 100 h test in NH_3, improved from 0.008 V h^{-1} to 0.0022 V h^{-1} (0.5 A cm^{-2} 650 °C)[67] Power density: 1.08× increase in NH_3 (443 mW cm^{-2} to 479 mW cm^{-2} at 800 °C); degradation rate: 120 h test in NH_3 at 100 mA cm^{-2}, improved from 0.063 V h^{-1} → 0.00089 V h^{-1} at 700 °C (ref. 81)
Exsolution	Reductive conditions drive metal-ions to exsolve from host oxide lattices (*e.g.*, perovskites), yielding anchored nanoparticles	Robust metal–support interactions; superior anti-sintering, anti-coking, and anti-nitridation stability	Restricted to electrolyte-supported architectures (compromised performance); challenging particle-size and alloy control	Optimal for durable, anchored catalysts, albeit at initial performance expense	Power density: 1.3× increase (288 mW cm^{-2} to 374 mW cm^{-2} at 800 °C); degradation rate: 322 h test in NH_3, improved by 8% (100 mA cm^{-2},800 °C)[72] Power density: 2× increase in CH_4 (250 mW cm^{-2} to 500 mW cm^{-2} at 500 °C); degradation rate: 500 h test in CH_4 at 0.75 V, improved 20-fold (0.4%/h to 0.02%/h at 500 °C)[90]
Atomic layer deposition	Sequential, self-limiting surface reactions afford atomic-precision, conformal film growth	Angstrom-level thickness control; exceptional uniformity/conformality; tunable surface chemistry	Slow deposition rates; costly precursors/equipment; scale-up hurdles	Premier for nanoscale porous anode engineering, enabling precise catalytic/protective coatings	Power density: 2× increase (0.16 W cm^{-2} to 0.34 W cm^{-2} at 500 °C in NH_3); degradation rate: 100 h test in NH_3 at 0.3 A cm^{-2}, 500 °C, improved from 17% to 2% (ref. 66) Power density: activation resistance decreases by 31% (52.6 Ω cm^{-2} to 36.2 Ω cm^{-2} at 450 °C in CH_4)[134]

ammonia decomposition forms Ni_3N, which diminishes conductivity and induces cracking through volume expansion. These effects intensify below 600 °C owing to sluggish ammonia cracking.[64,65] Reported degradation rates include 29.4%/100 h for Ni–YSZ anodes at 700 °C,[61] 20%/100 h at 700 °C (0.2 A cm^{-2}),[65] and 2%/100 h for PdNi-BZCYYb anodes at 500 °C (0.3 A cm^{-2}).[66] All substantially exceed the DOE target of <0.2% per 1000 h, which was often improved by one to three orders of magnitude due to ammonia induced nitridation/oxidation mechanisms absent in H_2 systems. Advanced strategies such as FeNi (3.9%/100 h)[67] or RuCuNi (1.36%/100 h)[68] offer improvements but seldom achieve targets, as confirmed in comprehensive surveys.[69]

3. Surface modification techniques: a comparative framework

A range of surface modification techniques has been explored to address these challenges.[70–76] Table 1 provides a comparative overview of their characteristics relative to SOFC anode requirements.

3.1. Infiltration

Infiltration represents a versatile strategy for augmenting the catalytic performance and durability of SOFC anodes.[61,67,77–84] This approach entails impregnating a porous scaffold, typically Ni–YSZ, with a precursor solution of the target catalyst, followed by calcination or reduction to yield finely dispersed nanoparticles that enhance surface reaction kinetics without disrupting the anode's bulk architecture. Its appeal lies in operational simplicity, low cost, and compatibility with high activity promoters.

Infiltration has been widely exploited to engineer anode architecture for DM- and DA-SOFCs. Hua *et al.* realized a protonic ceramic fuel cell with exceptional performance and fuel flexibility by infiltrating a $PrBaMn_2O_{5+\delta}$ (PBM) double perovskite together with Ni_4Co bimetallic nanoparticles into a Ni–$BaZr_{0.1}Ce_{0.7}Y_{0.1}Yb_{0.1}O_{3-\delta}$ (Ni–BZCYYb) anode (Fig. 2a and

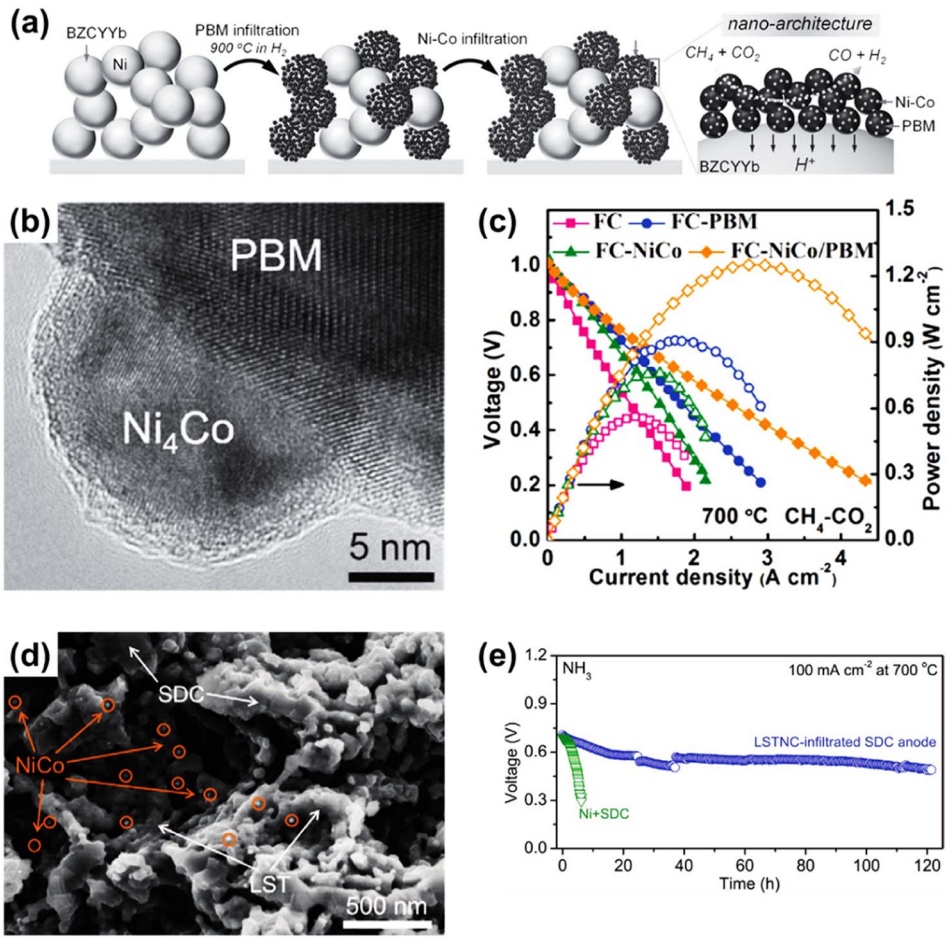

Fig. 2 Infiltration as a surface modification strategy for direct methane (DM)- and direct ammonia (DA)- solid oxide fuel cell (SOFC) anodes. (a) Schematic illustration of the preparation of a NiCo/$PrBaMn_2O_{5+\delta}$ (NiCo/PBM) bifunctional nanoarchitecture on $BaZr_{0.1}Ce_{0.7}Y_{0.1}Yb_{0.1}O_{3-\delta}$ within a porous Ni-based cermet anode. (b) High-resolution transmission electron microscopy image of an infiltrated Ni_4Co nanoparticle on the PBM scaffold. (c) Current–voltage and power density characteristics of the corresponding cells at 700 °C using a CH_4–CO_2 fuel mixture. Reproduced with permission.[83] Copyright 2016, Wiley-VCH. (d) Scanning electron microscopy image of a NiCo-infiltrated $La_{0.55}Sr_{0.30}TiO_{3-\delta}$–$Sm_{0.2}Ce_{0.8}O_{2-\delta}$ (LST–SDC) anode. (e) Operational stability of the DA-SOFCs employing a reduced $La_{0.52}Sr_{0.28}Ti_{0.94}Ni_{0.03}Co_{0.03}O_{3-\delta}$-infiltrated SDC compared with a conventional Ni–SDC anode at a current density of 100 mA cm^{-2} at 700 °C. Reproduced with permission.[81] Copyright 2020, Wiley-VCH.

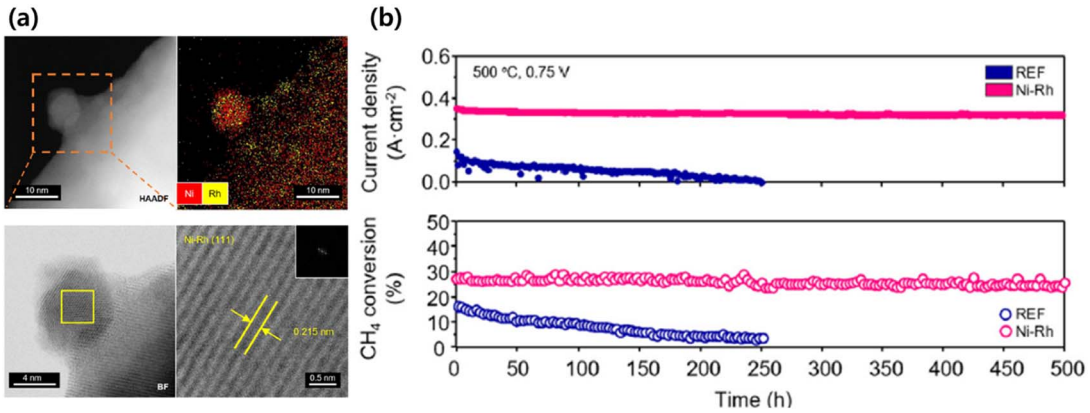

Fig. 3 Exsolution as a surface modification strategy for direct methane solid oxide fuel cells (DM-SOFCs). (a) Structure and chemical composition of the catalyst on the fuel electrode determined by transmission electron microscopy and energy dispersive X-ray spectroscopy mapping with lattice spacing images for the Ni–Rh cell. (b) Long-term stability evaluations of electrochemical performance and catalytic activity for 500 h at 500 °C, where the direct methane proton conducting SOFC operated with a fuel composition of 25% CH_4, 25% H_2O, and 50% Ar at the fuel electrode at a constant cell voltage of 0.75 V. Reproduced with permission.[90] Copyright 2023, Springer Nature.

b).[83] The preferential deposition of PBM on BZCYYb grains promoted *in situ* methane reforming, while the Ni_4Co nanocatalyst enhanced reforming and electro-oxidation kinetics, enabling efficient direct-methane utilization and suppressing degradation associated with CO_2 exposure (Fig. 2c).[83]

Building on this strategy, Song *et al.* showed that NiCo alloy nanoparticles infiltrated into a $La_{0.55}Sr_{0.30}TiO_{3-\delta}$ (LST) perovskite scaffold markedly improved ammonia decomposition and mitigated nanoparticle sintering, affording stable DA-SOFC operation for 120 h (Fig. 2d and e).[81] Rathore *et al.* infiltrated Pd into an LSCF-Ag composite anode for DA-SOFCs, achieving a 43% increase in power density relative to the Pd-free analogue, attributed to accelerated hydrogen dissolution and ammonia-cracking kinetics.[84] Xu *et al.* reported $CeO_{2-\delta}$ nanoparticle infiltration into Ni–YSZ anodes, delivering a peak power density of 0.941 W cm^{-2} at 700 °C with improved durability.[61] He *et al.* demonstrated that Pd-doped BZCYYb substantially enhanced both ammonia decomposition and proton conductivity, yielding 724 mW cm^{-2} at 650 °C.[82] Zhang *et al.* further showed that Fe-modified Ni–BZCYYb anodes strengthened ammonia adsorption and facilitate nitrogen desorption, enabling a peak power density of 1.609 W cm^{-2} at 700 °C.[67]

Despite these advances, infiltration remains fundamentally limited by long-term stability concerns, as nanoparticle sintering and agglomeration progressively diminish catalytic activity under extended operation. Spatially nonuniform catalyst distribution can further introduce cell-to-cell and intra-electrode performance variability, while the repeated cycles of impregnation and high-temperature treatment pose intrinsic challenges for scale-up and manufacturing reproducibility. These constraints highlight the need for next-generation surface-engineering strategies that afford superior control over catalyst morphology and robustness, as discussed later.

3.2. Exsolution

Exsolution offers a robust strategy for elevating SOFC anode performance through the reductive precipitation of catalytically active nanoparticles from a host oxide lattice.[85–91] Distinct from infiltration, this process fosters intimate metal–support interactions that confer exceptional resistance to nanoparticle sintering. Typically, transition metals (*e.g.*, Ni, Fe, and Ru) are incorporated into perovskite or Ruddlesden–Popper structures, exsolving as discrete surface nanoparticles under reducing conditions, aiming to facilitate methane reforming reactions.[92–97]

Recent advances include the work of Hong *et al.*, who realized a self-assembled Ni–Rh bimetallic catalyst for direct-methane protonic ceramic fuel cells, combining high methane conversion with excellent durability.[90] In this architecture, Ni is exsolved onto a Rh-decorated BZCYYb surface to form a highly active Ni–Rh alloy layer (Fig. 3a), which promotes hydrogen spillover and accelerates water–gas-shift chemistry, enabling peak power densities of 1.13 W cm^{-2} at 650 °C and 0.50 W cm^{-2} at 500 °C, together with a degradation rate of only 0.02%/h over 500 h, approximately twenty-fold lower than that in conventional H-SOFCs (Fig. 3b).

Several studies have investigated DA-SOFC anodes employing exsolution to enhance performance and stability.[95–98] Xiong *et al.* demonstrated that slight Ru substitution in $Pr_{0.6}Sr_{0.4}Co_{0.2}Fe_{0.8}O_{3-\delta}$ (PSCFRu) promotes dense exsolution of CoFeRu nanocatalysts (approximately 400 particles per μm^2, with a size of 20 nm, see Fig. 4a) compared to the Ru-free analogue (approximately 100 particles per μm^2, with a size of 50 nm), yielding a peak power density of 374 mW cm^{-2} at 800 °C (Fig. 4b), substantially higher than 288 mW cm^{-2} of the reduced PSCF anode and stable operation for >322 h, whereas conventional Ni–SDC and r-PSCF electrodes degraded rapidly (Fig. 4c).[72] Cavazzani *et al.* showed that Ni exsolved from $La_{0.45}Sr_{0.45}Ti_{0.9}Ni_{0.1}O_3$ (LSTNO) dramatically outperformed

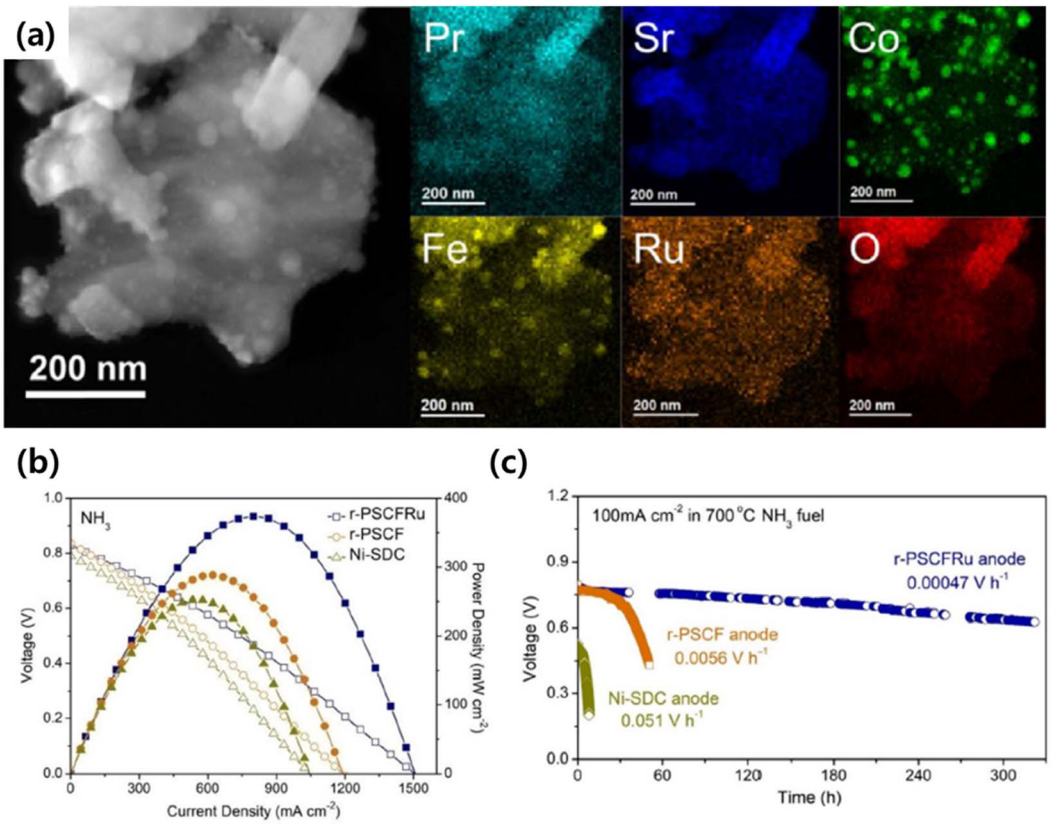

Fig. 4 Exsolution as a surface modification strategy for direct ammonia solid oxide fuel cells (DA-SOFCs). (a) Scanning tunneling electron microscopy image and energy dispersive X-ray spectroscopy mapping of exsolved CoFeRu alloy nanoparticles formed on a $Pr_{0.6}Sr_{0.4}Co_{0.2}Fe_{0.75}Ru_{0.05}O_{3-\delta}$ (PSCFRu) perovskite anode. (b) Current–voltage and power density characteristics of DA-SOFCs operated at 800 °C. (c) Long-term stability using ammonia fuel at a constant current density of 100 mA cm^{-2} and 700 °C. Reproduced with permission.[72] Copyright 2022, Elsevier.

both bare and Ni-infiltrated $La_{0.45}Sr_{0.45}TiO_3$ (LSTO) anodes, lowering the polarization resistance in NH_3 from 65.5 Ω cm^2 (bare) and 43.7 Ω cm^2 (infiltrated) to 12.2 Ω cm^2 (exsolved) at 800 °C, through the formation of uniformly dispersed, strongly anchored Ni nanoparticles that afford superior metal–support interaction, charge/mass transport, and thermochemical robustness relative to infiltrated Ni, which readily aggregates and degrades.[99]

Yi *et al.* further exploited NiCo exsolution in $Sr_2CoMo_{1-x}Ni_xO_{6-\delta}$ (SCMN) double perovskites for DA-SOFCs, identifying $Sr_2CoMo_{0.8}Ni_{0.2}O_{6-\delta}$ (r-SCMN2) as an optimum composition that delivers 350 mW cm^{-2} at 800 °C in NH_3 and exhibits 250 h of operation with a low voltage decay of 0.74 mV h^{-1}, outperforming both other SCMN variants and Ni–SDC anodes.[91]

Exsolution, however, also has intrinsic limitations that constrain its practical impact. As noted above, the absolute performance of exsolved ceramic-based anodes remains inferior to that of Ni/YSZ or Ni/BZCYYb anodes because of the inherently lower catalytic activity of ceramic-based electrodes, despite their markedly improved stability. In addition, the high reduction temperatures required for exsolution limit compatibility with many electrode and electrolyte chemistries, thereby narrowing the accessible materials space. The density and spatial distribution of exsolved nanoparticles are largely governed by the bulk composition and reduction conditions, which hinder independent optimization of these parameters. Even strongly anchored nanoparticles can undergo coarsening or partial detachment under prolonged operation, leading to a gradual loss of activity. Moreover, noble metals that are particularly effective for methane cracking (*e.g.*, Pt) or ammonia decomposition (*e.g.*, Ru) are often difficult to incorporate into perovskite electrodes as single phases and typically do not exsolve quantitatively, leaving a fraction trapped in the lattice and limiting both loading control and catalytic utilization.

4. Opportunities of atomic layer deposition in surface modification techniques over infiltration and exsolution

4.1. Fundamentals of ALD

Given these challenges, infiltration and exsolution, though effective, suffer from inherent limitations in precise control over surface composition, morphology, and long-term stability. An alternative surface modification technique, atomic layer deposition (ALD), provides a promising route for engineered

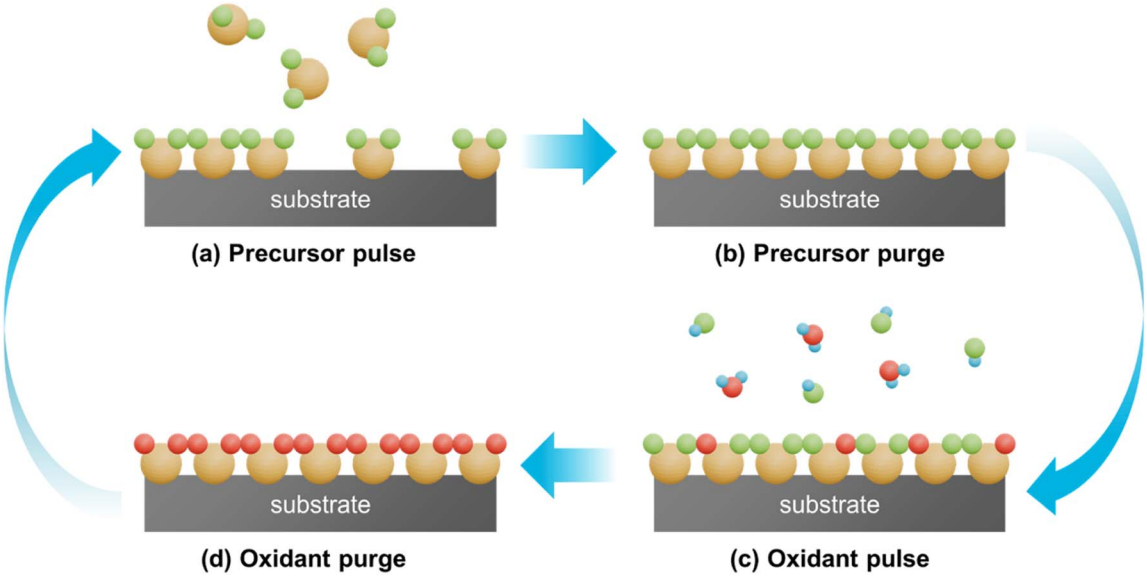

Fig. 5 Schematic illustration of the atomic layer deposition process. (a) Precursor pulse; (b) precursor purge; (c) oxidant pulse; (d) oxidant purge.

catalytic coating. ALD proceeds through a cyclic sequence of self-limiting gas–solid reactions consisting of a precursor pulse, precursor purge, oxidant pulse, and oxidant purge. During the precursor pulse (see Fig. 5a), volatile precursor molecules are introduced into the reactor and chemisorb onto reactive surface sites of the substrate to form a saturated monolayer, while excess precursor remains in the gas phase. In the subsequent precursor purge step (Fig. 5b), an inert carrier gas removes unreacted precursor molecules and volatile by-products from the chamber, preventing any parasitic gas phase reactions. In

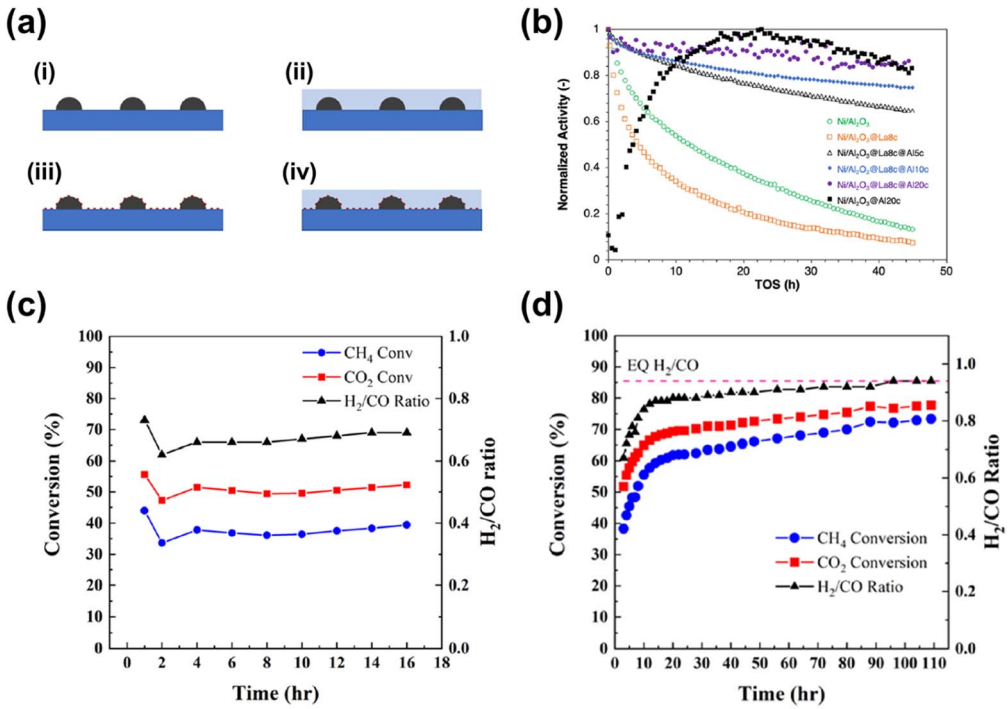

Fig. 6 Enhancement of Ni-catalyzed methane dry reforming (DRM) reactivity by atomic layer deposition (ALD) of (doped) Al_2O_3 overcoats. (a) Schematic of the La_2O_3-doped Al_2O_3 ALD sequence on Ni/Al_2O_3: (i) pristine Ni nanoparticles, (ii) Ni@ Al_2O_3 (20 cycles), (iii) Ni@ La_2O_3 (8 cycles), (iv) Ni@La_2O_3(8 cycles)@Al_2O_3(20 cycles). (b) Time-on-stream (TOS) normalized CH_4 reforming rates (700 °C), highlighting suppressed deactivation for the La_2O_3/Al_2O_3-overcoated catalyst. Reproduced with permission.[108] Copyright 2022, American Chemical Society. Dry methane reforming performance of 5 wt% Ni/CeO_2–ZrO_2–Al_2O_3 (CZA) (c) before and (d) after 0.5 nm Al_2O_3 ALD overcoating (750 °C, 1.2 bar, 10 900/h GHSV). Reproduced with permission.[109] Copyright 2024, American Chemical Society.

the oxidant pulse (Fig. 5c), an oxidizing reactant is supplied and reacts selectively with the chemisorbed precursor species, converting them into the desired solid film and regenerating reactive surface groups that are chemically equivalent to the initial state. A second purge step with an inert gas (Fig. 5d) then eliminates residual oxidant and reaction byproducts, restoring a clean gaseous environment. By repeating this four-step cycle, the film grows in a layer-by-layer fashion with sub-nanometer thickness control, excellent conformality over high-aspect-ratio structures, and high uniformity across the substrate. The following section examines how ALD overcomes the shortcomings of conventional infiltration and exsolution while delivering enhanced structural stability and catalytic performance.

4.2. ALD as an activator and stabilizer of Ni catalysts for methane reforming

ALD of ultrathin oxide overcoating on Ni-based anodes emerges as a transformative approach for direct-methane SOFC fuel electrodes, delivering precise control and superior performance over infiltration methods. While infiltration effectively introduces promoters such as $(Sm,Ce)O_{2-\delta}$ or La_2O_3 into Ni–YSZ structures to boost reforming and extend stability at 600–800 °C, ALD's self-limiting, conformal deposition of Al_2O_3, CeO_2, or FeO_x layers provides sub-nanometer precision that uniquely encapsulates Ni nanoparticles.[100–105] This physical confinement prevents Ostwald ripening and sintering while engineering oxygen-vacancy-rich interfaces for efficient CO_2/H_2O dissociation and coke gasification.[106,107] Unlike broader infiltration distributions, ALD minimizes active-site blockage through atomically thin shells, suppressing reverse water–gas shift and graphitic coke formation for optimized syngas quality. This scalability positions ALD as an ideal strategy for high-performance, coke-resistant SOFC anodes tailored to direct methane operation.

Al_2O_3, the archetypal ALD-deposited material, effectively suppresses Ni sintering and coking. However, $NiAl_2O_4$ interphase formation deteriorates Ni's catalytic activity. As demonstrated in the schematic illustration of sequential ALD by Ahn *et al.* (Fig. 6a), pre-deposition of La_2O_3 *via* ALD prevented $NiAl_2O_4$ formation.[108] The resultant La_2O_3–Al_2O_3 overcoat preserves peak activity, eliminates the protracted (~20 h) induction period, and delivers exceptional lifetime under methane reforming conditions (see Fig. 6b). La_2O_3 sites remodel the overlayer to maximize Ni surface exposure while anchoring mobile Ni atoms, achieving stability without activity loss.

In conventional DM-SOFCs, Ni catalysts reside on oxygen-storage supports (*e.g.*, YSZ, doped ceria) exhibiting high oxygen mobility. Lucas *et al.* investigated ALD Al_2O_3 (~0.5 nm) overlayers on Ni supported by redox-active CeO_2–ZrO_2–Al_2O_3

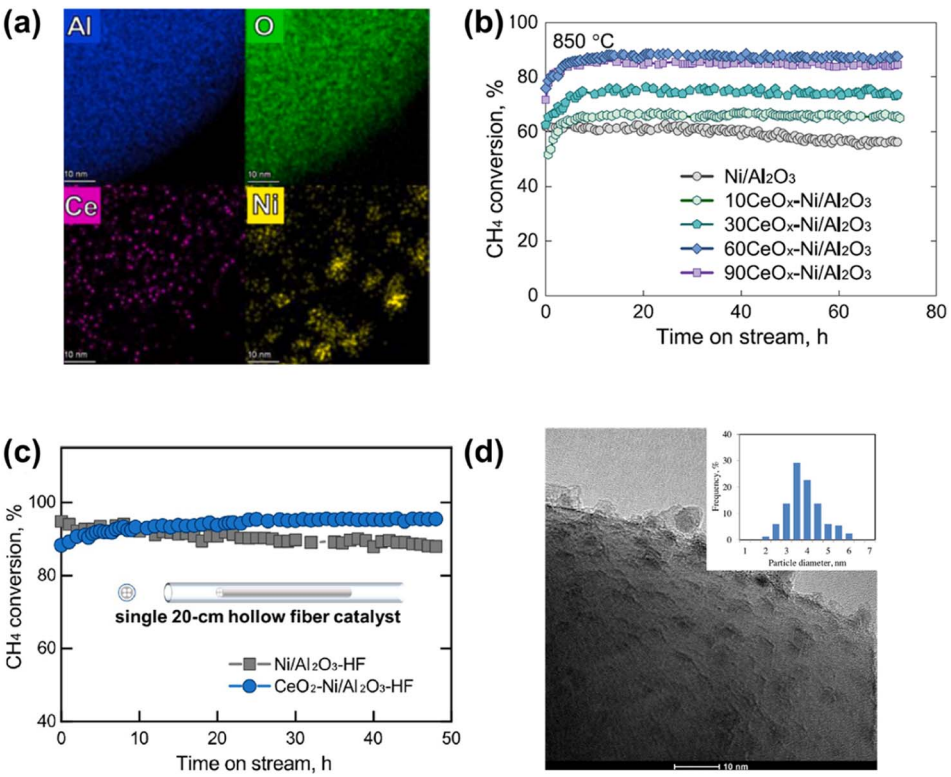

Fig. 7 Extended applications of atomic layer deposition (ALD) for Ni methane reforming catalyst optimization. (a) Energy-dispersive X-ray spectroscopy elemental mapping of Ni/Al_2O_3 with a CeO_x ALD overcoat. (b) CH_4 conversion *versus* time-on-stream for pristine and CeO_x-coated Ni/Al_2O_3 (850 °C). Reproduced with permission.[110] Copyright 2023, Elsevier. (c) CH_4 conversion for pristine and CeO_2-promoted 20 cm-long hollow-fiber Ni/Al_2O_3 catalysts. Reproduced with permission.[111] Copyright 2022, American Chemical Society. (d) Transmission electron microscopy image of an ALD Ni/Al_2O_3 catalyst. Reproduced with permission.[112] Copyright 2017, Elsevier.

(CZA) mixed oxides.[109] While the pristine Ni/CZA catalyst exhibited relatively low reactivity (Fig. 6c), this modification enhances Ni dispersion, curtails coking by >10-fold, suppresses the reverse water–gas shift (lowering H_2 yield), and enables >140 h of stable methane reforming operation with 77% CH_4 conversion (Fig. 6d).

Jin *et al.* reported that CeO_x, another prototypical ALD-deposited material, also significantly enhances methane reforming.[110] By tuning ALD conditions (primarily temperature), oxygen-deficient CeO_x overlayers shown in Fig. 7a are achieved that enhance Ni reducibility, balance $CH_4/CO_2/H_2O$ activation, and suppress coking *via* timely carbon oxidation. This delivers dramatically improved activity, optimal H_2/CO selectivity, and long-term stability under demanding conditions (700–850 °C, see Fig. 7b). Unlike the limited conformal coverage of sputtering, ALD enables scalable deposition on high-aspect-ratio structured supports such as 20 cm-long multichannel γ-Al_2O_3 hollow fibers, portending applicability to complex SOFC anode architectures (Fig. 7c). Uniform ~4 nm Ni nanoparticles are deposited within high-aspect-ratio channels and pores, maximizing dispersion and accessibility as shown in Fig. 7c, while still retaining their ability to stabilize Ni catalysts. Ni particle size critically governs reforming performance and coking resistance. Shang *et al.* demonstrated that ALD yields highly dispersed Ni nanoparticles (2–4 nm, see Fig. 7d), below the threshold for carbon nucleation, with 1.6 wt% loadings on Ni/Al_2O_3 delivering balanced activity and superior anti-coking performance *versus* conventional catalysts plagued by larger particles and rapid deactivation.[112]

4.3. ALD as a uniform nanocatalyst coater for ammonia decomposition

Enhancing the NH_3 decomposition rate is most effectively achieved by dispersing uniform Ni or Ru nanoparticles, the most active elements for this reaction.[113] Compared to infiltration and exsolution methods, ALD offers superior conformal coating of nanoscale particles. Notably, unlike exsolution, in which Ru remains partially embedded in the lattice, ALD ensures full utilization of precious Ru on the surface.

In this manner many studies have been conducted on utilization of ALD for ammonia decomposition and precious metal nanoparticle decoration.[118–126] Yang *et al.* demonstrated ALD of Ni clusters on CeO_2 nanorods as highly active catalysts for NH_3 decomposition (Fig. 8a), achieving an ultrahigh H_2 production rate of 954.2 mmol per g_{Ni} per min at 550 °C, surpassing most Ni-based catalysts (Fig. 8b).[114] Unlike Ni single atoms from impregnation, which incorporate into the CeO_2 lattice and bind N adatoms too strongly, impeding nitrogen desorption (the rate-determining step), ALD Ni clusters form $Ni–O_v–Ce^{3+}$ interfacial sites *via* strong metal–support interactions. These electron-enriched Ni sites weaken Ni–N bonds, facilitating NH_3 activation and associative N_2 desorption.

As shown in Fig. 8c, Nakatsubo *et al.* demonstrated that the novel Ru(TMM)p-cymene precursor, characterized by its small and simple molecular structure, facilitates highly uniform Ru deposition *via* ALD on complex, high-aspect-ratio (aspect ratio 4) trench structures on TiN substrates.[115] This process achieves excellent step coverage of 95% and conformal, dense films

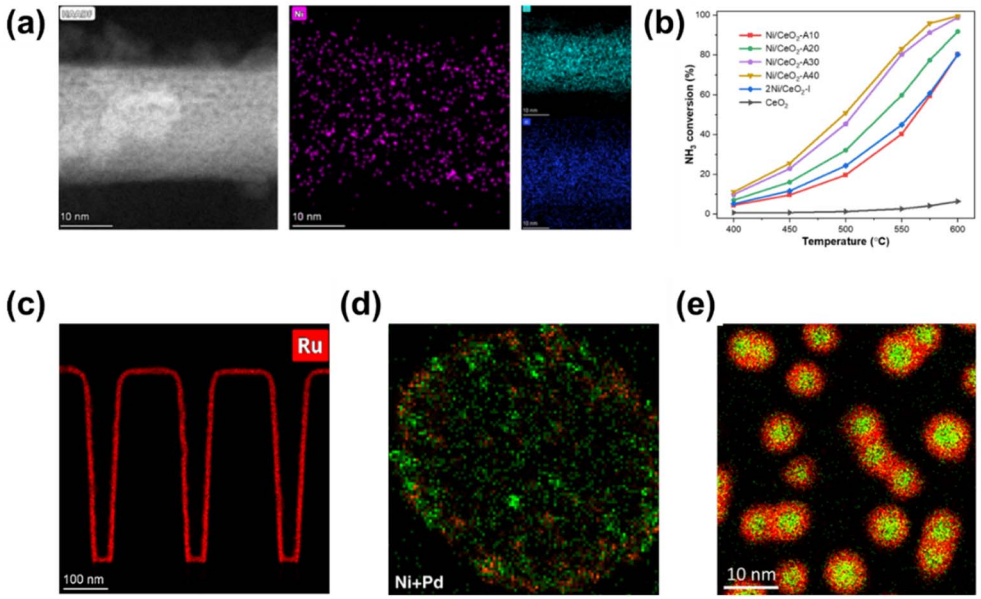

Fig. 8 Utilization of atomic layer deposition (ALD) for the fabrication of nanocatalysts with exceptional uniformity and dispersion. (a) High-angle annular dark-field scanning transmission electron microscopy (HAADF-STEM) images and corresponding energy-dispersive X-ray spectroscopy (EDS) elemental maps of Ni nanoparticles deposited on a CeO_2 support *via* ALD. (b) Catalytic performance of Ni/CeO_2 catalysts toward NH_3 decomposition. Reproduced with permission.[114] Copyright 2025, American Chemical Society. EDS elemental maps: (c) Ru deposited on a trenched substrate illustrating the conformal nature of ALD, (d) Pd nanocatalysts grown on Ni nanoparticles, and (e) Pt deposited on Pd nanoparticles by ALD. Reproduced with permission.[115–117] Copyright 2025, Wiley-VCH. Copyright 2019, Springer-Nature. Copyright 2015, IOPscience.

with thicknesses down to 10 nm. The observed uniformity arises from the precursor's exceptional thermal stability up to 400 °C and a high growth per cycle of 1.28 Å per cycle. Fig. 8d and e illustrates Pd deposition on Ni catalysts and the encapsulation of Pd nanoparticles with Pt shells, respectively, both enabled by ALD. These results highlight the potential of ALD for sophisticated nanocatalyst engineering aimed at enhancing the ammonia decomposition performance of DA-SOFC anodes.

4.4. ALD applied to DM- and DA-SOFCs

4.4.1 Fabrication of ALD-modified SOFCs. ALD offers exceptional flexibility in the SOFC fabrication sequence. As illustrated in Fig. 9, ALD can typically be introduced in the following steps: (Fig. 9a and b) after full sintering of the anode support and electrolyte layers (Fig. 9a and b), thereby preserving the microstructure and porosity of the sintered body at the powder level, or prior to sintering, using particle-by-particle (powder) ALD (Fig. 9c).

The choice of sequence depends on the coating function and processing constraints. Powder ALD ensures complete surface modification of primary particles and is ideal for introducing barrier or promoter layers before densification. However, ALD coating done post-sintering is advantageous when conformal coatings (*e.g.*, <10 nm of Ru, Pd, CeO_2, or Al_2O_3) are required on high-aspect-ratio pore networks for catalytic enhancement, redox stability, or coke/nitridation suppression.

As illustrated in Fig. 9, the post-sintering ALD route begins after the porous electrode is formed on an electrolyte substrate, typically *via* screen-printing and co-sintering at 1000–1400 °C. The ALD process, conducted at low temperature (typically <250 °C), then deposits nanometric coatings conformally onto the internal surfaces of the porous scaffold without altering its bulk structure. Two representative modes are illustrated: surface nanoparticle decoration, where catalytically active nanoclusters are deposited throughout the pore network; and conformal oxide thin-film coating, which encapsulates the backbone while preserving porosity and gas pathways (Fig. 9). This approach is compatible with standard SOFC processing since it occurs after all high-temperature sintering steps.

From a geometrical and transport standpoint, the feasibility of ALD within porous SOFC electrodes is dictated by three primary factors: precursor diffusion length, pore throat diameter, and structural tortuosity. In typical SOFC anodes, dominant pore diameters range from 0.1 to 1 μm. Within this range, ultrathin ALD coatings in the sub-10 nm regime occupy only a few percent of the pore radius, introducing only modest reductions in transport cross-section, provided that growth remains conformal and does not overfill narrow necks or bottlenecks.[76,127]

Quantitative conformality studies on high-aspect-ratio substrates, particularly from the battery field, have confirmed that nanometer-scale ALD coatings are compatible with both mesoporous and macro-porous architectures. For example, Zazpe *et al.* demonstrated that uniform ALD films could penetrate several micrometers into pores with diameters of 50–200 nm and aspect ratios exceeding 100 : 1, given sufficient precursor exposure and purge times.[128] Similarly, Sharma *et al.* achieved conformal deposition of ZnO and Al_2O_3 into anodic aluminum oxide (AAO) membranes and commercial Li-ion battery electrodes with 100–200 nm pores and up to 40 μm thickness, confirming that <10 nm coatings can fully infiltrate deep porous networks without clogging the structure, as long as flow dynamics are properly tuned.[129]

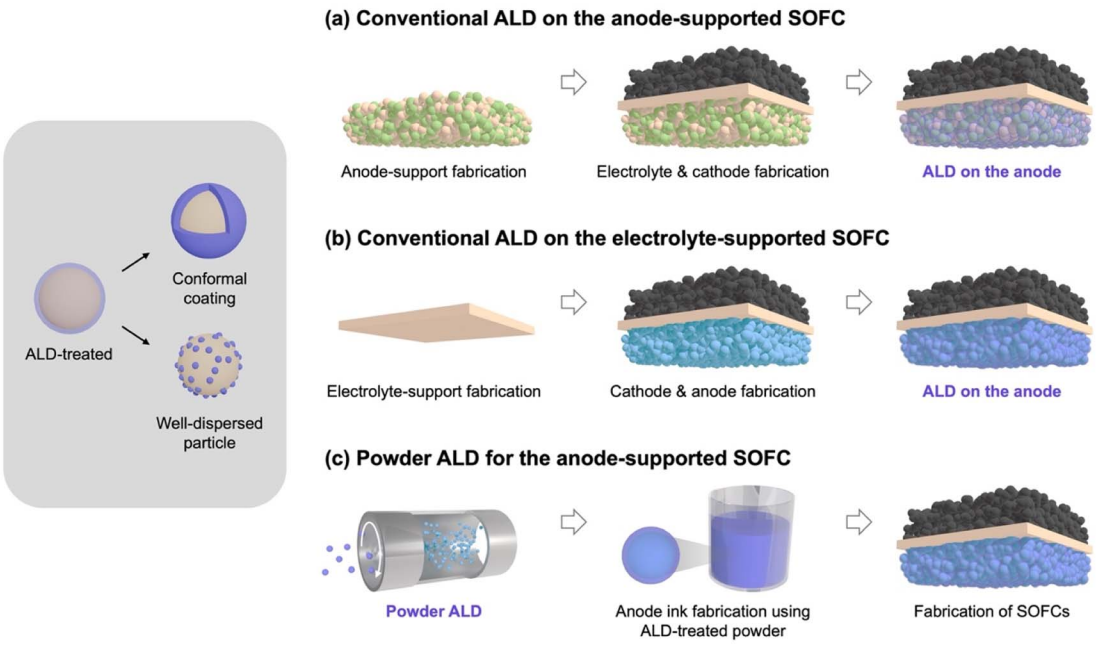

Fig. 9 Schematic illustration of the fabrication process of solid oxide fuel cells modified by atomic layer deposition. (a) Conventional ALD on the anode-supported SOFC. (b) Conventional ALD on the electrolyte-supported SOFC. (c) Powder ALD for the anode-supported SOFC.

Modeling efforts reinforce these findings. Fang *et al.* showed that typical ALD precursors like trimethylaluminum (TMA) or metal amidinates exhibit characteristic penetration depths of ~5–10 μm per exposure cycle in 50–100 nm-wide trench geometries under standard pulsing conditions.[130] In realistic SOFC anodes with pore widths around 50 nm and overall thickness ~30 μm, this suggests that deep and uniform coating is feasible but demands extended pulse times, elevated precursor partial pressures, or pulsed-pressure (stop-flow) delivery.

However, these studies also highlight a key scaling constraint: as the pore size decreases, from 100 nm to 50 nm or below, the accessible penetration depth of ALD coatings drops sharply, due to both the quadratic dependence of diffusion time on pore diameter and enhanced flow resistance from tortuous pathways. Practically, this means that in thick or complex SOFC anodes, it is advisable to limit ALD thicknesses to ~2–10 nm and to implement optimized exposure protocols (*e.g.*, longer pulses and static exposure steps) to ensure that the narrowest transport constrictions remain open while still enabling functional catalytic or protective coverage.

Recent work by Yu *et al.* further confirms that even sub-5 nm ALD films can successfully infiltrate and modify perovskite-based scaffolds with mesopores below 50 nm,[131] enhancing interfacial properties without compromising permeability, underscoring that ALD can be effectively deployed in high-aspect-ratio porous energy devices across diverse electrochemical platforms.

Gas permeability is preserved when the ALD coating thickness remains below ~10–15% of the local pore diameter. For SOFC anodes with average pore sizes of 50–200 nm, this corresponds to coatings of approximately 3–10 nm, which aligns well with the typical thickness range of catalytic or protective ALD layers such as Ru, Pd, CeO_2, or Al_2O_3. For instance, Jo *et al.* applied ~4 nm Ru ALD films to SDC anodes and observed no significant change in the polarization resistance, indicating that mass transport and triple-phase boundary access were maintained.[132] This suggests that with careful thickness control, ALD coatings can enhance electrode functionality without impeding the gas flow.

Maintaining permeability, however, involves a trade-off: coatings must be sufficiently thick to achieve the desired catalytic or barrier effects, yet thin enough to avoid narrowing the smallest transport pathways.[127] Pore-scale modeling and experimental studies have shown that, under Knudsen-diffusion dominated transport, modest reductions in pore diameter from conformal ALD films primarily reduce effective diffusivity but do not drastically impair flow, unless the coating closes narrow necks.[129] This emphasizes the need to tailor the ALD thickness based on the most constricted features, not just the average pore size. In practice, 2–10 nm coatings are generally optimal for SOFC anodes, whereas thicker films (>20 nm) should be limited to electrodes with relatively large (>0.5–1 μm), well-connected porosity.[130]

To improve precursor penetration in tortuous geometries, ALD variants such as plasma-enhanced ALD (PEALD) or stop-flow (exposure) modes are used. These approaches increase conformality by prolonging reactant residence time and enabling full surface saturation, especially in thick or high-aspect ratio structures. Stop valves and long purge steps also help avoid gas-phase reactions that could lead to pore blockage.[76]

From a processing standpoint, ALD is well-aligned with SOFC fabrication. Most oxide and metal ALD processes operate between 80 and 250 °C, far below the sintering temperatures of common materials like YSZ, GDC, and Ni-based cermets (≥1000 °C), enabling post-sintering integration without disturbing the microstructure. PEALD and spatial ALD further reduce processing temperatures (<150–200 °C) and cycle times, making them suitable for post-assembly modifications or even stack-level treatments.[131]

Powder-level ALD, while beneficial for coating unsintered particles uniformly, must be carefully managed to avoid undesired phase reactions during sintering. For example, Al_2O_3 coatings on Ni can lead to $NiAl_2O_4$ spinel formation at high temperatures; thus, protective interlayers such as La_2O_3 are often introduced to prevent this. Therefore, the choice between pre- or post-sintering ALD depends on the desired functional location, thermal stability, and material interactions.

Ultimately, ensuring both gas permeability and fabrication compatibility requires a coordinated design of pore architecture, ALD chemistry, and deposition strategy. Systematic studies that integrate microstructural statistics, coating penetration depth, and gas transport measurements across ALD-treated SOFC electrodes remain an important direction for future research.

4.4.2 Applications of ALD-modified SOFCs. With its capability to form gas-permeable protective conformal layers and to deposit uniformly distributed precious metal nanocatalysts, ALD has already demonstrated strong potential for enhancing the performance of direct-fueled SOFCs. Kye *et al.* reported the use of plasma-enhanced ALD (PEALD) deposited Ru nanoparticles on SDC and Ni–SDC anodes to simultaneously enhance methane oxidation kinetics and carbon coking resistance.[133] They applied ultralow loading Ru catalysts (<10 μg cm^{-2}) using plasma-enhanced ALD on anodes for a methane oxidation electrode (Fig. 10a). The PEALD process produced highly dense Ru nanoparticles with a large surface area and increased the Ru–SDC interface (*i.e.*, triple-phase boundary, TPB) density. Compared to sputtered Ru, PEALD Ru nanoparticles penetrated well into the porous SDC or Ni–SDC anode. Electrochemical analysis revealed that the PEALD Ru@SDC cell with optimized Ru thickness outperformed the sputtered Ru@SDC cell, despite reducing precious metal loading by ~95%. Furthermore, PEALD Ru enhanced cell stability by suppressing carbon coking, facilitating carbon removal processes, and altering carbon bonding. Similarly, in the same group, Go *et al.*, applied the PEALD Ru nanoparticles on the Ni–SDC anode for DM-SOFCs.[134] They also confirmed that decoration of ~4 nm-thick Ru on the Ni–SDC anode reduced the activation resistance by 31%, and promoted the carbon removal process, mitigating carbon coking at the anode. This enhancement appears to result from the improved methane reforming and/or

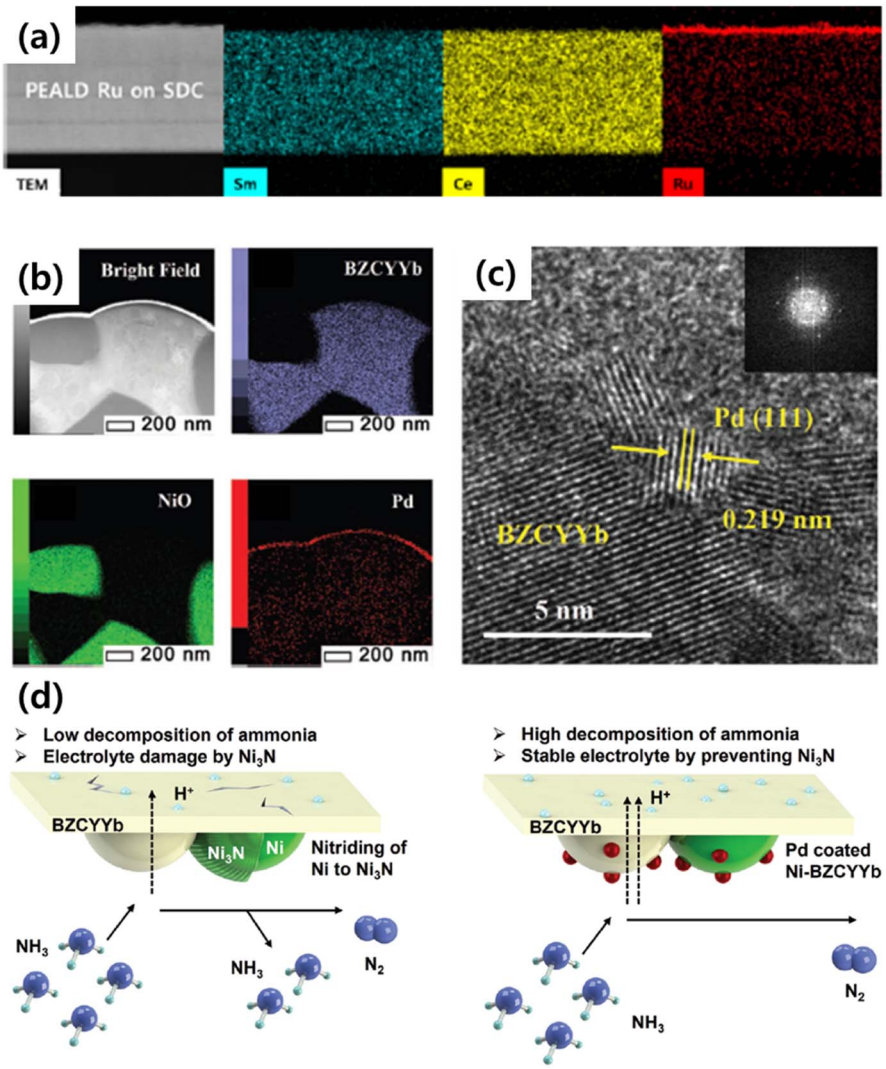

Fig. 10 Application of atomic layer deposition (ALD) to the anodes of direct methane (DM-) and direct ammonia (DA-) solid oxide fuel cells (SOFCs). (a) Cross-sectional transmission electron microscopy (TEM) and energy dispersive X-ray spectroscopy (EDS) mapping images of plasma enhanced ALD Ru on the $Sm_{0.2}Ce_{0.8}O_{2-\delta}$ anode for DM-SOFCs. Reproduced with permission.[133] Copyright 2021, American Chemical Society. (b) TEM-EDS mapping images of ALD Pd on the NiO-BZCYYb anode for DA-SOFCs. (c) High resolution-TEM characterization of the ALD Pd deposited anode. (d) Degradation reactions due to structural deformations of the PCFCs caused by nitriding reactions of Ni. Schematic model of the nitriding reaction of Ni in the bare sample of the PCFCs (without Pd) (left) and Pd-treated PCFCs (right). Reproduced with permission.[66] Copyright 2023, Wiley-VCH.

oxidation reactions occurring at the closely interacting Ni–Ru and SDC–Ru interfaces, facilitated by the plasma-based ALD.

Jeong *et al.* were the first to apply ALD for anode surface modification in DA-SOFCs, demonstrating the superior advantages of ALD compared to traditional techniques such as infiltration and sputtering.[66] They deposited a highly uniform Pd catalyst layer on the anode surface using the ALD process, significantly enhancing fuel cell performance under ammonia fuel conditions. The ALD process ensured excellent permeability and conformal coating across the porous anode structure, resulting in a nearly twofold improvement in peak power density, reaching 340 mW cm^{-2} at 500 °C. Impedance analysis revealed that the ALD-Pd treatment effectively reduced polarization resistance and improved current collection, particularly in the low-temperature regime, making it a viable approach for enhancing SOFC efficiency. Moreover, ALD-modified Pd catalysts effectively suppressed the formation of Ni_3N, a critical issue in DA-SOFCs, thereby improving the long-term stability of the anode. This suppression can be attributed to the Pd particles surrounding the Ni sites, which hinder the nitridation reaction between Ni and ammonia, preventing the formation of Ni_3N that leads to structural degradation (Fig. 10d). As a result, the Pd-coated anode retained its integrity over prolonged operation, reducing performance degradation and enhancing the overall durability of the DA-SOFCs.

5. Challenges and future perspectives

Despite significant advancements in ALD-based surface modification of SOFC anodes, several challenges remain before this

technique can be fully integrated into commercial SOFC systems. Future research must focus on addressing scalability, material optimization, cost-effectiveness, and long-term stability to enable the widespread adoption of ALD-based anode modifications in direct-fueled SOFCs.

One of the most critical areas for future research is improving scalability, cost-effectiveness, and material versatility. ALD's inherently slow deposition rate and the high cost of many metal–organic precursors remain major barriers to large-scale manufacturing, while the limited number of reported studies on mixed ionic–electronic conductors (MIECs) and perovskite-based anodes further constrains material selection. Developing high-throughput ALD techniques, such as spatial ALD, roll-to-roll ALD, and plasma-enhanced ALD (PEALD), could substantially enhance deposition efficiency while maintaining film conformality and thickness control. In parallel, the exploration of low-cost precursors, optimization of process conditions to reduce energy consumption, and expansion of compatible MIEC and perovskite chemistries will be essential.

Another key research priority is the development of multifunctional ALD coatings tailored to specific fuel environments. Incorporating novel materials such as bimetallic catalysts (*e.g.*, Pt–Ru), doped oxides (*e.g.*, Gd-doped CeO_2), and multilayer architectures (*e.g.*, Al_2O_3/ZrO_2) offers opportunities to simultaneously enhance catalytic activity and mitigate degradation mechanisms including carbon deposition, sulfur poisoning, and nitridation. Rational design of such coatings, in which catalytic layers are integrated with protective oxide barriers, could significantly improve anode durability and performance stability under harsh operating conditions.

Integrating ALD with other surface modification strategies represents another promising direction. The high uniformity and atomic-scale thickness control afforded by ALD can be combined with exsolution approaches to generate self-regenerating anodes with enhanced long-term catalytic activity. Similarly, ALD-assisted infiltration of catalytic nanoparticles into porous anode frameworks may maximize triple-phase boundary density and improve fuel oxidation kinetics. Hybrid strategies that integrate ALD with conventional sintering and screen-printing processes should also be explored to facilitate scalability and industrial implementation.

Techno-economic analysis and industrial feasibility studies are essential to assess the commercial viability of ALD-based anode modifications. Future research should include comprehensive cost assessments and life-cycle analyses to evaluate the long-term economic benefits of ALD-enhanced anodes. Moreover, investigating the impact of ALD modifications on full SOFC stack performance, rather than relying solely on single-cell studies, will be critical for determining their effectiveness at the system level.

Finally, long-term durability studies under realistic operating conditions are required to validate the practical potential of ALD-modified anodes. While most ALD processes are conducted at relatively low temperatures, typically below 300 °C, the thermal and chemical stability of ALD-derived phases during subsequent high-temperature reduction, thermal cycling, and extended operation remains insufficiently understood. Future work should therefore focus on identifying degradation pathways specific to ALD-modified anodes, assessing material compatibility across different fabrication sequences and developing strategies to mitigate long-term performance losses in direct-fueled SOFC environments.

By addressing these challenges, ALD can become a key enabler for next-generation SOFCs, offering enhanced anode stability, improved fuel conversion efficiency, and long-term durability. However, achieving this goal requires continued advancements in process scalability, material innovation, and cost reduction strategies to fully integrate ALD into commercial SOFC systems. Future studies should focus on developing industrial-scale ALD systems, optimizing hybrid fabrication techniques, and conducting extensive durability testing to accelerate the transition from research to real-world deployment.

6. Conclusion

The development of direct methane and ammonia solid oxide fuel cells promises high-efficiency, fuel-flexible energy conversion, yet commercialization is hindered by carbon deposition, sulfur poisoning, nitridation, and anode instability. Challenges persist in ALD scalability (slow rates and precursor costs) and long-term durability under realistic conditions, demanding high-throughput variants (spatial and roll-to-roll ALD) and hybrid strategies with exsolution/infiltration. Addressing these *via* material innovation, process optimization, and techno-economic analysis will enable ALD to transform next-generation SOFCs for sustainable energy.

Author contributions

Hao-Yang Li: investigation (lead), writing – original draft (lead), writing – review & editing (lead). Hyunseung Kim: investigation (lead), writing – review & editing (lead). Jeong Woo Shin: writing – original draft (lead). Jiyoon Shin: investigation (lead), writing – original draft (supporting). Pei-Chen Su: supervision (lead), writing – review & editing (lead).

Conflicts of interest

We declare no conflict of interest.

Data availability

This is a review article. No new data were created or analysed in this study. Data sharing is not applicable to this article.

Acknowledgements

The project was supported by the National Research Foundation, Prime Minister's Office, Singapore, under its Campus for Research Excellence and Technological Enterprise (CREATE) program, as part of the Grand Challenge on Decarbonization with Ammonia Using SOFC for Power Generation.

References

1 B. C. Steele and A. Heinzel, *Nature*, 2001, **414**, 345–352.
2 O. Yamamoto, *Electrochim. Acta*, 2000, **45**, 2423–2435.
3 A. B. Stambouli and E. Traversa, *Renew. Sustain. Energy Rev.*, 2002, **6**, 433–455.
4 N. Q. Minh, *Solid State Ionics*, 2004, **174**, 271–277.
5 H. G. Seo, H. Kim, W. Jung and H. L. Tuller, *Appl. Catal., B*, 2024, **355**, 124172.
6 H. Kim, H. G. Seo, S. Ahn, H. L. Tuller and W. Jung, *J. Mater. Chem. A*, 2025, **13**, 9708–9714.
7 J. Liu, J. K. Kim, Y. Wang, H. Kim, A. Belotti, B. Koo, Z. Wang, W. C. Jung and F. Ciucci, *Energy Environ. Sci.*, 2022, **15**, 4069–4082.
8 I. Dincer and C. Acar, *Int. J. Hydrogen Energy*, 2014, **40**, 11094–11111.
9 C. Acar and I. Dincer, *Int. J. Hydrogen Energy*, 2014, **39**, 1–12.
10 Y. Lin, Z. Zhan, J. Liu and S. A. Barnett, *Solid State Ionics*, 2005, **176**, 1827–1835.
11 W. Wang, C. Su, Y. Wu, R. Ran and Z. Shao, *Chem. Rev.*, 2013, **113**, 8104–8151.
12 G. Cinti, G. Discepoli, E. Sisani and U. Desideri, *Int. J. Hydrogen Energy*, 2016, **41**, 13583–13590.
13 Q. Xu, Z. Guo, L. Xia, Q. He, Z. Li, I. Temitope Bello, K. Zheng and M. Ni, *Energy Convers. Manag.*, 2022, **253**, 115175.
14 S. S. Rathore, S. Biswas, D. Fini, A. P. Kulkarni and S. Giddey, *Int. J. Hydrogen Energy*, 2021, **46**, 35365–35384.
15 E. P. Murray, T. Tsai and S. A. Barnett, *Nature*, 1999, **400**, 649–651.
16 A. Fuerte, R. X. Valenzuela, M. J. Escudero and L. Daza, *J. Power Sources*, 2009, **192**, 170–174.
17 Z. Wan, Y. Tao, J. Shao, Y. Zhang and H. You, *Energy Convers. Manag.*, 2021, **228**, 113729.
18 T. M. Gür, *Prog. Energy Combust. Sci.*, 2016, **54**, 1–64.
19 P. Qiu, S. Sun, X. Yang, F. Chen, C. Xiong, L. Jia and J. Li, *Int. J. Hydrogen Energy*, 2021, **46**, 25208–25224.
20 L. Fan, C. Li, P. V. Aravind, W. Cai, M. Han and N. Brandon, *J. Power Sources*, 2022, **538**, 231573.
21 H. Zhang, K. Xu, F. He, F. Zhu, Y. Zhou, W. Yuan, Y. Liu, M. Liu, Y. Choi and Y. Chen, *Adv. Mater.*, 2024, **36**, 2313966.
22 M. Asmare and M. Ilbas, *Int. J. Renew. Energy Technol.*, 2020, 70–91.
23 D. S. Dhawale, S. Biswas, G. Kaur and S. Giddey, *Inorg. Chem. Front.*, 2023, **10**, 6176–6192.
24 S. Souentie, M. Athanasiou, D. K. Niakolas, A. Katsaounis, S. G. Neophytides and C. G. Vayenas, *J. Catal.*, 2013, **306**, 116–128.
25 P. V. Aravind, T. Woudstra, N. Woudstra and H. Spliethoff, *J. Power Sources*, 2009, **190**, 461–475.
26 E. S. Hecht, G. K. Gupta, H. Zhu, A. M. Dean, R. J. Kee, L. Maier and O. Deutschmann, *Appl. Catal., A*, 2005, **295**, 40–51.
27 N. Nakagawa, H. Sagara and K. Kato, *J. Power Sources*, 2001, **92**, 88–94.
28 H. Timmermann, D. Fouquet, A. Weber, E. Ivers-Tiffée, U. Hennings and R. Reimert, *Fuel Cells*, 2006, **6**, 307–313.
29 D. L. King, J. J. Strohm, X. Q. Wang, H. S. Roh, C. Wang, Y. H. Chin, Y. Wang, Y. Lin, R. Rozmiarek and P. Singh, *J. Catal.*, 2008, **258**, 356–365.
30 J. Yang, A. F. S. Molouk, T. Okanishi, H. Muroyama, T. Matsui and K. Eguchi, *ACS Appl. Mater. Interfaces*, 2015, **7**, 28701–28707.
31 K. Miyazaki, T. Okanishi, H. Muroyama, T. Matsui and K. Eguchi, *J. Power Sources*, 2017, **365**, 148–154.
32 S. S. Shy, S. C. Hsieh and H. Y. Chang, *J. Power Sources*, 2018, **396**, 80–87.
33 P. C. Wu and S. S. Shy, *J. Power Sources*, 2017, **362**, 105–114.
34 Q. Ma, R. R. Peng, L. Tian and G. Meng, *Electrochem. Commun.*, 2006, **8**, 1791–1795.
35 A. N. Zainon, M. R. Somalu, A. M. Kamarul Bahrain, A. Muchtar, N. A. Baharuddin, M. A. Muhammed, N. Osman, A. Abdul Samat, A. K. Azad and N. P. Brandon, *Int. J. Hydrogen Energy*, 2023, **48**, 20441–20464.
36 L. Shu, J. Sunarso, S. S. Hashim, J. Mao, W. Zhou and F. Liang, *Int. J. Hydrogen Energy*, 2019, **44**, 31275–31304.
37 J. S. Kim, V. V. Nair, J. M. Vohs and R. J. Gorte, *Scr. Mater.*, 2011, **65**, 90–95.
38 M. Bilal Hanif, M. Motola, S. qayyum, S. Rauf, A. khalid, C.-J. Li and C.-X. Li, *Chem. Eng. J.*, 2022, **428**, 132603.
39 W. Akimoto, T. Fujimoto, M. Saito, M. Inaba, H. Yoshida and T. Inagaki, *Solid State Ionics*, 2014, **256**, 1–4.
40 H. T. Huang, D. C. Lu, C. X. Li and S. L. Zhang, *Int. J. Hydrogen Energy*, 2024, **87**, 89–99.
41 S. Kim, C. Kim, J. H. Lee, J. Shin, T. H. Lim and G. Kim, *Electrochim. Acta*, 2017, **225**, 399–406.
42 M. R. Cesario, G. S. Souza, F. J. A. Loureiro, A. J. M. Araújo, J. P. F. Grilo, S. Aouad, H. L. Tidahy, D. A. Macedo, D. P. Fagg, C. Gennequin and E. Abi-Aad, *Ceram. Int.*, 2021, **47**, 33191–33201.
43 H. Kim, C. Lu, W. L. Worrell, J. M. Vohs and R. J. Gorte, *J. Electrochem. Soc.*, 2002, **149**, A247.
44 B. J. M. Sarruf, J. E. Hong, R. Steinberger-Wilckens and P. E. V. de Miranda, *Int. J. Hydrogen Energy*, 2020, **45**, 5297–5308.
45 O. Rahumi, Y. Yuferov, L. Meshi, N. Maman and K. Borodianskiy, *J. Power Sources*, 2025, **631**, 236320.
46 W. Zhang and Y. H. Hu, *Energy Sci. Eng.*, 2023, **11**, 3276–3288.
47 H. J. Kim, M. J. Kil, J. Lee, B. C. Yang, D. Go, Y. Lim, Y.-B. Kim and J. An, *Appl. Surf. Sci.*, 2021, **538**, 148105.
48 M. M. Whiston, I. M. L. Azevedo, S. Litster, C. Samaras, K. S. Whitefoot and J. F. Whitacre, *Joule*, 2019, **3**, 2060–2065.
49 R. H. Crabtree, *Chem. Rev.*, 1995, **95**, 987–1007.
50 H. Schwarz, *Angew. Chem., Int. Ed.*, 2011, **50**, 10096–10115.
51 J.-H. Koh, Y.-S. Yoo, J.-W. Park and H. C. Lim, *Solid State Ionics*, 2002, **149**, 157–166.
52 H. Li, W. Wei, T. Zhang, F. Liu, X. Xu, Z. Li and Z. Liu, *Appl. Energy*, 2024, **359**, 122609.
53 M. Zendrini, M. Testi, M. Trini, P. Daniele, J. Van Herle and L. Crema, *Int. J. Hydrogen Energy*, 2021, **46**, 30112–30123.

54 A. Afif, N. Radenahmad, Q. Cheok, S. Shams, J. H. Kim and A. K. Azad, *Renew. Sustain. Energy Rev.*, 2016, **60**, 822–835.
55 Y. Luo, S. Liao, S. Chen, H. Fang, F. Zhong, L. Lin, C. Zhou, C. Chen, G. Cai, C. T. Au and L. Jiang, *Appl. Energy*, 2022, **307**, 118158.
56 R. Lan and S. Tao, *Front. Energy Res.*, 2014, **2**, 1–4.
57 H. Zhang, R. Xiong, Z. Chen, Z. Cheng, J. Huang, B. Sa, N. Ai, L. Zhang, S. H. Chan, C. Guan, Y. Chen, S. P. Jiang and K. Chen, *Adv. Funct. Mater.*, 2025, 1–10.
58 A. M. Abdalla, A. T. Azad, A. B. Madian, L. A. Omeiza, Y. Subramanian, B. Wei, J. Taweekun, M. M. Khairat Dawood and A. K. Azad, *Environ. Sci. Pollut. Res.*, 2024, **31**, 46769–46789.
59 O. Elmutasim, S. Giddey, D. S. Dhawale and S. Bhattacharya, *Int. J. Hydrogen Energy*, 2024, **96**, 192–209.
60 G. Jeerh, M. Zhang and S. Tao, *J. Mater. Chem. A*, 2021, **9**, 727–752.
61 K. Xu, F. Zhu, M. Hou, C. Li, H. Zhang and Y. Chen, *Nano Res.*, 2023, **16**, 2454–2462.
62 M. Morales, M. A. Laguna-Bercero and E. Jiménez-Piqué, *J. Eur. Ceram. Soc.*, 2023, **43**, 2740–2751.
63 X. Jiang, X. Lei, F. Liang, J. Mao, L. Shu and W. Zhou, *Int. J. Hydrogen Energy*, 2026, **199**, 152834.
64 Y. Ya, Y. shu Xu, A. M. Elbanna, Y. Liu, B. Sun and X. Cheng, *Renew. Sustain. Energy Rev.*, 2025, **213**, 115350.
65 V. Singh, H. Muroyama, T. Matsui and K. Eguchi, *ECS Trans.*, 2017, **78**, 2527–2536.
66 H. J. Jeong, W. Chang, B. G. Seo, Y. S. Choi, K. H. Kim, D. H. Kim and J. H. Shim, *Small*, 2023, **19**, e2208149.
67 H. Zhang, Y. Zhou, K. Pei, Y. Pan, K. Xu, Y. Ding, B. Zhao, K. Sasaki, Y. Choi, Y. Chen and M. Liu, *Energy Environ. Sci.*, 2022, **15**, 287–295.
68 H. Zhang, K. Xu, Y. Xu, F. He, F. Zhu, K. Sasaki, Y. M. Choi and Y. Chen, *Energy Environ. Sci.*, 2024, **17**, 3433–3442.
69 H. Lee, J. Baek and M. Choi, *J. Mater. Chem. A*, 2025, **13**, 20080–20103.
70 J. M. Vohs and R. J. Gorte, *Adv. Mater.*, 2009, **21**, 943–956.
71 S. P. Jiang, *Mater. Sci. Eng., A*, 2006, **418**, 199–210.
72 X. Xiong, J. Yu, X. Huang, D. Zou, Y. Song, M. Xu, R. Ran, W. Wang, W. Zhou and Z. Shao, *J. Mater. Sci. Technol.*, 2022, **125**, 51–58.
73 H. Jeong, Y. H. Kim, B.-R. Won, H. Jeon, C. Park and J. Myung, *Chem. Mater.*, 2023, **35**, 3745–3764.
74 D. Neagu, J. T. S. Irvine, J. Wang, B. Yildiz, A. K. Opitz, J. Fleig, Y. Wang, J. Liu, L. Shen, F. Ciucci, B. A. Rosen, Y. Xiao, K. Xie, G. Yang, Z. Shao, Y. Zhang, J. Reinke, T. A. Schmauss, S. A. Barnett, R. Maring, V. Kyriakou, U. Mushtaq, M. N. Tsampas, Y. Kim, R. O'Hayre, A. J. Carrillo, T. Ruh, L. Lindenthal, F. Schrenk, C. Rameshan, E. I. Papaioannou, K. Kousi, I. S. Metcalfe, X. Xu and G. Liu, *J. Phys.: Energy*, 2023, **5**, 031501.
75 R. W. Johnson, A. Hultqvist and S. F. Bent, *Mater. Today*, 2014, **17**, 236–246.
76 V. Cremers, R. L. Puurunen and J. Dendooven, *Appl. Phys. Rev.*, 2019, **6**, 021302.
77 M. Li, B. Hua, J. L. Luo, S. P. Jiang, J. Pu, B. Chi and L. Jian, *J. Mater. Chem. A*, 2015, **3**, 21609–21617.
78 A. Wang, T. Li, X. Wang, Z. Li, X. Huang, Y. Yin, S. Zhu, B. Liu and L. Jia, *Ceram. Int.*, 2023, **49**, 25240–25245.
79 K. Hong, S. N. Sutanto, J. A. Lee and J. Hong, *J. Mater. Chem. A*, 2021, **9**, 6139–6151.
80 L. Liu, K. Sun, X. Wu, X. Li, M. Zhang, N. Zhang and X. Zhou, *Int. J. Hydrogen Energy*, 2012, **37**, 10857–10865.
81 Y. Song, H. Li, M. Xu, G. Yang, W. Wang, R. Ran, W. Zhou and Z. Shao, *Small*, 2020, **16**, 2001859.
82 F. He, Q. Gao, Z. Liu, M. Yang, R. Ran, G. Yang, W. Wang, W. Zhou and Z. Shao, *Adv. Energy Mater.*, 2021, **11**, 2003916.
83 B. Hua, N. Yan, M. Li, Y. Sun, Y. Zhang, J. Li, T. Etsell, P. Sarkar and J. Luo, *Adv. Mater.*, 2016, **28**, 8922–8926.
84 S. S. Rathore, A. P. Kulkarni, D. Fini, S. Giddey and A. Seeber, *Solids*, 2021, **2**, 177–191.
85 Z. Sun, C. Hao, S. Toan, R. Zhang, H. Li, Y. Wu, H. Liu and Z. Sun, *J. Mater. Chem. A*, 2023, **11**, 17961–17976.
86 F. Liu, H. Deng, Z. Wang, A. J. M. Hussain, N. Dale, Y. Furuya, Y. Miura, Y. Fukuyama, H. Ding, B. Liu and C. Duan, *J. Am. Chem. Soc.*, 2024, **146**, 4704–4715.
87 J. Cavazzani, E. Squizzato, E. Brusamarello and A. Glisenti, *Int. J. Hydrogen Energy*, 2022, **47**, 13921–13932.
88 X. Xiong, J. Yu, X. Huang, D. Zou, Y. Song, M. Xu, R. Ran, W. Wang, W. Zhou and Z. Shao, *J. Mater. Sci. Technol.*, 2022, **125**, 51–58.
89 O. Kwon, S. Joo, S. Choi, S. Sengodan and G. Kim, *J. Phys.: Energy*, 2020, **2**, 032001.
90 K. Hong, M. Choi, Y. Bae, J. Min, J. Lee, D. Kim, S. Bang, H.-K. Lee, W. Lee and J. Hong, *Nat. Commun.*, 2023, **14**, 7485.
91 Y. Yi, J. Chen, M. Xu, G. Yang, R. Ran, W. Zhou, W. Wang and Z. Shao, *Catalysts*, 2023, **13**, 996.
92 J. Zhang, M. Li, F. Jin, J. Zhang, R. Li, X. Li, Y. Gao, X. Ou and Y. Ling, *Int. J. Hydrogen Energy*, 2024, **55**, 572–580.
93 S. Vecino-Mantilla, P. Gauthier-Maradei, M. Huvé, J. M. Serra, P. Roussel and G. H. Gauthier, *ChemCatChem*, 2019, **11**, 4631–4641.
94 S. Vecino-Mantilla, P. Gauthier-Maradei, M. Huvé, J. M. Serra, P. Roussel and G. H. Gauthier, *ChemCatChem*, 2019, **11**, 4631–4641.
95 S. Y. Batool, M. H. Hassan, S. U. Rehman, H.-S. Kim, R.-H. Song, T.-H. Lim, D. W. Joh, S.-J. Park, J.-E. Hong and S.-B. Lee, *ACS Appl. Energy Mater.*, 2025, **8**, 2452–2464.
96 F. Zhong, L. Wang, H. Fang, Y. Luo, C. Chen, L. Lin, K. Chen and L. Jiang, *Chem. Eng. J.*, 2023, **471**, 144650.
97 J. Ha, J. Choi, J. Maeng, G. H. Park, J. Ji, S. Choi, N. Kim, S. Jeong and W. B. Kim, *Chem. Eng. J.*, 2025, **522**, 168167.
98 W. Jang, H. Jeong, Y. H. Kim, J.-E. Hong and J. Myung, *Chem. Eng. J.*, 2025, **525**, 170247.
99 J. Cavazzani, E. Squizzato, E. Brusamarello and A. Glisenti, *Int. J. Hydrogen Energy*, 2022, **47**, 13921–13932.
100 E. Baktash, P. Littlewood, R. Schomäcker, A. Thomas and P. C. Stair, *Appl. Catal., B*, 2015, **179**, 122–127.
101 S. Afzal, A. V. Prakash, P. Littlewood, T. J. Marks, E. Weitz, P. C. Stair and N. O. Elbashir, *Int. J. Hydrogen Energy*, 2020, **45**, 12835–12848.

102 T. D. Gould, M. M. Montemore, A. M. Lubers, L. D. Ellis, A. W. Weimer, J. L. Falconer and J. W. Medlin, *Appl. Catal., A*, 2015, **492**, 107–116.
103 B. Jin, K. Wang, H. Yu, X. He and X. Liang, *Chem. Eng. J.*, 2023, **459**, 141611.
104 P. Littlewood, S. Liu, E. Weitz, T. J. Marks and P. C. Stair, *Catal. Today*, 2020, **343**, 18–25.
105 S. Ahn, T. J. Marks and P. C. Stair, *Catal. Today*, 2026, **463**, 115609.
106 U. Guharoy, T. R. Reina, J. Liu, Q. Sun, S. Gu and Q. Cai, *J. CO_2 Util.*, 2021, **53**, 101728.
107 N. Pham-Ngoc, A. Jamsaz, Y. Lee, E.-S. Oh and E. W. Shin, *Chem. Eng. J.*, 2025, **510**, 161545.
108 S. Ahn, P. Littlewood, Y. Liu, T. J. Marks and P. C. Stair, *ACS Catal.*, 2022, **12**, 10522–10530.
109 J. Lucas, N. S. Padmanabha Naveen, M. J. Janik, K. Alexopoulos, G. Noh, D. Aireddy, K. Ding, J. A. Dorman and K. M. Dooley, *ACS Catal.*, 2024, **14**, 9115–9133.
110 B. Jin, K. Wang, H. Yu, X. He and X. Liang, *Chem. Eng. J.*, 2023, **459**, 141611.
111 B. Jin, S. Li and X. Liang, *Ind. Eng. Chem. Res.*, 2022, **61**, 10377–10386.
112 Z. Shang, S. Li, L. Li, G. Liu and X. Liang, *Appl. Catal., B*, 2017, **201**, 302–309.
113 T. Su, B. Guan, J. Zhou, C. Zheng, J. Guo, J. Chen, Y. Zhang, Y. Yuan, W. Xie, N. Zhou, H. Dang, B. Xu and Z. Huang, *Energy Fuels*, 2023, **37**, 8099–8127.
114 Z. Yang, Z. Shui, M. Zhao, Z. Wei, F. Zhang, X. Duan, B. Niu, B. Li, G. Jiang and Z. Hao, *ACS Catal.*, 2025, **15**, 6255–6265.
115 H. Nakatsubo, D. Mohapatra, E. S. Lee, J. Kim, I. Cho, M. Iseki, T. Shigetomi, R. Harada, S. W. Na, T. Cheon, B. Shong and S. H. Kim, *Adv. Sci.*, 2025, e19209.
116 H. Wang, Q. Luo, W. Liu, Y. Lin, Q. Guan, X. Zheng, H. Pan, J. Zhu, Z. Sun, S. Wei, J. Yang and J. Lu, *Nat. Commun.*, 2019, **10**, 4998.
117 M. J. Weber, M. A. Verheijen, A. A. Bol and W. M. M. Kessels, *Nanotechnology*, 2015, **26**, 094002.
118 H. Feng, J. A. Libera, P. C. Stair, J. T. Miller and J. W. Elam, *ACS Catal.*, 2011, **1**, 665–673.
119 H. Feng, J. W. Elam, J. A. Libera, W. Setthapun and P. C. Stair, *Chem. Mater.*, 2010, **22**, 3133–3142.
120 C. Lausecker, D. Muñoz-Rojas and M. Weber, *Crit. Rev. Solid State Mater. Sci.*, 2024, **49**, 908–930.
121 D. Z. Austin, M. A. Jenkins, D. Allman, S. Hose, D. Price, C. L. Dezelah and J. F. Conley, *Chem. Mater.*, 2017, **29**, 1107–1115.
122 M. F. J. Vos, S. N. Chopra, M. A. Verheijen, J. G. Ekerdt, S. Agarwal, W. M. M. Kessels and A. J. M. Mackus, *Chem. Mater.*, 2019, **31**, 3878–3882.
123 J.-Y. Park, S. Yeo, T. Cheon, S.-H. Kim, M.-K. Kim, H. Kim, T. E. Hong and D.-J. Lee, *J. Alloys Compd.*, 2014, **610**, 529–539.
124 J. W. Elam, A. Zinovev, C. Y. Han, H. H. Wang, U. Welp, J. N. Hryn and M. J. Pellin, *Thin Solid Films*, 2006, **515**, 1664–1673.
125 J. J. Senkevich, F. Tang, D. Rogers, J. T. Drotar, C. Jezewski, W. A. Lanford, G. -C. Wang and T. -M. Lu, *Chem. Vap. Deposition*, 2003, **9**, 258–264.
126 T. Aaltonen, P. Alén, M. Ritala and M. Leskelä, *Chem. Vap. Deposition*, 2003, **9**, 45–49.
127 W. Szmyt, C. Guerra-Nuñez, L. Huber, C. Dransfeld and I. Utke, *Chem. Mater.*, 2022, **34**, 203–216.
128 R. Zazpe, J. Prikryl, V. Gärtnerova, K. Nechvilova, L. Benes, L. Strizik, A. Jäger, M. Bosund, H. Sopha and J. M. Macak, *Langmuir*, 2017, **33**, 3208–3216.
129 K. Sharma, D. Routkevitch, N. Varaksa and S. M. George, *J. Vac. Sci. Technol., A*, 2016, **34**, 01A146.
130 W.-Z. Fang, Y.-Q. Tang, C. Ban, Q. Kang, R. Qiao and W.-Q. Tao, *Chem. Eng. J.*, 2019, **378**, 122099.
131 B. Yu, J. Zhang, Y. Yang, D. Yu, Y. Mai and X. Chen, *Energy Mater.*, 2024, **4**, 400045.
132 S. E. Jo, S. Jeon, H. J. Kim, B. C. Yang, K. Ju, T. M. Gür, W. Jung and J. An, *Small Methods*, 2024, **8**, 1–10.
133 S. Kye, H. J. Kim, D. Go, B. C. Yang, J. W. Shin, S. Lee and J. An, *ACS Catal.*, 2021, **11**, 3523–3529.
134 D. Go, T. Kim, H. Li, T. Garcia, B. C. Yang, T. M. Gür, M. H. Lee and J. An, *Surf. Interfaces*, 2024, **44**, 103657.